Constraining the Equation of State of Neutron Stars from Binary Mergers

Kentaro Takami,[1] Luciano Rezzolla,[1,2] and Luca Baiotti[3]
[1]Institut für Theoretische Physik, Max-von-Laue-Straße 1, 60438 Frankfurt, Germany
[2]Max-Planck-Institut für Gravitationsphysik, Albert Einstein Institut, Am Mühlenberg 1, 14476 Potsdam, Germany
[3]Graduate School of Science and Institute of Laser Engineering, Osaka University, 5600043 Toyonaka, Japan
(Received 24 March 2014; published 28 August 2014)

Determining the equation of state of matter at nuclear density and hence the structure of neutron stars has been a riddle for decades. We show how the imminent detection of gravitational waves from merging neutron star binaries can be used to solve this riddle. Using a large number of accurate numerical-relativity simulations of binaries with nuclear equations of state, we find that the postmerger emission is characterized by two distinct and robust spectral features. While the high-frequency peak has already been associated with the oscillations of the hypermassive neutron star produced by the merger and depends on the equation of state, a new correlation emerges between the low-frequency peak, related to the merger process, and the total compactness of the stars in the binary. More importantly, such a correlation is essentially universal, thus providing a powerful tool to set tight constraints on the equation of state. If the mass of the binary is known from the inspiral signal, the combined use of the two frequency peaks sets four simultaneous constraints to be satisfied. Ideally, even a single detection would be sufficient to select one equation of state over the others. We test our approach with simulated data and verify it works well for all the equations of state considered.

DOI: 10.1103/PhysRevLett.113.091104 PACS numbers: 04.25.D-, 04.25.dk, 04.30.Db, 26.60.Kp

Introduction.—This decade is likely to witness the first direct detection of gravitational waves (GWs) as a series of advanced detectors such as LIGO [1], Virgo [2], and KAGRA [3] become operational in the next five years. Among the sources of GWs expected to be detected are the inspiral and postmerger of neutron-star binaries or neutron-star–black-hole binaries, and binary black holes. Population-synthesis models suggest that binary neutron star mergers (BNSs) may be the most common source, with an expected detection rate of $\sim 40\ \mathrm{yr}^{-1}$ [4].

Any GW signal from a binary including a neutron star will contain important signatures of the equation of state (EOS) of matter at nuclear densities. A first signature is represented by the tidal corrections to the orbital phase; these are reasonably well understood analytically [5–7] and can be tracked accurately with advanced high-order numerical codes [8,9]. A second signature is instead related to the postmerger phase, where the object formed by the merger [most likely a hypermassive neutron star (HMNS)] can emit GWs in a narrow frequency range before collapsing to a black hole [10].

The first evidence that the information contained in the postmerger signal could be extracted from the corresponding spectrum was provided by Bauswein and Janka [11] (see also Refs. [12,13]), who performed a large number of simulations using a smoothed particle hydrodynamics code solving the Einstein field equations assuming conformal flatness, and employing a GW backreaction scheme within a post-Newtonian approximation (see also Ref. [14] for a subsequent general-relativistic study). Reference [11], in particular, pointed out the presence of a peak at high-frequency in the spectrum (dubbed f_{peak}) and showed it correlated with the properties of the EOS, e.g., with the radius of the maximum-mass nonrotating configuration. It was then recognized that f_{peak} corresponds to a fundamental fluid mode with $m = 2$ of the HMNS [15].

By performing a large number of accurate simulations in full general relativity of equal-mass and unequal-mass BNSs with a number of different nuclear EOSs, we have revisited the spectral properties of the postmerger GW signal. In this Letter we report our analysis of the spectral features with special attention to the low-frequency peak, which tracks the strong emission produced at the merger when the two dense stellar cores collide. We show that this peak has an essentially universal relation with the total compactness of the stars in the binary so that, combining the information from the two peaks, we can derive a simple and robust method to constrain the EOS.

Numerical setup.—Our results have been obtained in full general relativity solving the Einstein equations with the MCLACHLAN code [16,17]. The solution of the relativistic hydrodynamics equations is instead obtained using the WHISKY code [10,18]. The stars are modeled as obeying a nuclear EOS and we have considered five different models: i.e., APR4 [19], ALF2 [20], SLy [21], H4 [22], GNH3 [23]. Rather than using tables, it is more convenient to use n piecewise polytropic approximations to these EOSs [24], expressing the "cold" contribution to pressure and specific internal energy as $p_{\mathrm{c}} = K_i \rho^{\Gamma_i}$, $\epsilon_{\mathrm{c}} = \epsilon_i + K_i \rho^{\Gamma_i - 1}/(\Gamma_i - 1)$, where ρ and K are the rest-mass density and the polytropic

constant, respectively (see Ref. [25] for details); $n = 4$ is sufficient to obtain a rather accurate representation of the different EOSs.

In addition, to model the thermal effects arising from the merger, the cold pressure is augmented through an ideal-fluid EOS, so that the total pressure and specific internal energy are $p = p_c + p_{th}$, $\epsilon = \epsilon_c + \epsilon_{th}$, with $p_{th} = \rho\epsilon_{th}(\Gamma_{th} - 1)$ [26]. Following Ref. [27], we use $\Gamma_{th} = 2$, but we have verified that our results are not sensitive to this choice, with spectral differences that are a few percent at most when, for instance, $\Gamma_{th} = 1.8$ (a full analysis will be reported in a longer paper [28]). Finally, to span a larger range in stellar compactness and go beyond the one covered by the nuclear EOSs above, we have considered a sixth EOS given by a pure polytrope with $\Gamma = 2$ and $K = 123.6$ in units where $c = G = M_\odot = 1$.

For each EOS we have considered five equal-mass binaries with average (gravitational) mass at infinite separation in the range $\bar{M} \equiv (M_1 + M_2)/2 = (1.275$–$1.375)M_\odot$ for the APR4 EOS, $(1.225$–$1.325)M_\odot$ for the ALF2 EOS, $(1.250$–$1.350)M_\odot$ for the GNH3, H4, and SLy EOSs, and $(1.350$–$1.450)M_\odot$ for the $\Gamma = 2$ polytrope (higher masses would lead to short-lived HMNSs; additional properties of the binaries will be presented in the longer paper). We have also considered two unequal-mass binaries for the GNH3 and SLy EOSs having $\bar{M} = 1.300M_\odot$ and mass ratio $\simeq 0.92$. The binaries are modeled as irrotational in quasicircular orbits and computed with the LORENE code [29], assuming a conformally flat metric. To increase resolution we have employed a reflection symmetry across the $z = 0$ plane, a π-symmetry condition across the $x = 0$ plane (only for equal-mass binaries), and a moving-mesh refinement via the CARPET driver [30]. We have used six refinement levels, the finest having a resolution of $0.15M_\odot \simeq 0.221$ km, and extracted the GWs near the outer boundary at a distance $R_0 = 500\ M_\odot \simeq 738$ km.

Results.—As discussed by several authors [10–14,31], the power spectral density (PSD) of the postmerger GW signal exhibits a number of clear peaks. Two examples are presented in Fig. 1, which refers to two binaries with (gravitational) masses $\bar{M}/M_\odot = 1.325$, and APR4 and GNH3 EOSs. Since $h_+ \sim h_+^{22}$, the top panel shows the evolution of the $\ell = m = 2$ plus polarization of the strain aligned at the merger [32] for sources at a polar distance of 50 Mpc (dark-red and blue lines for the APR4 and GNH3 EOSs, respectively). The bottom panel, on the other hand, shows the spectral densities $2\tilde{h}(f)f^{1/2}$ windowed after the merger for the two EOSs, comparing them with the sensitivity curves of Advanced LIGO [33] (green line) and of the Einstein Telescope [34,35] (ET; light-blue line). The dotted lines refer to the whole time series and hence, where visible, indicate the power during the inspiral, while the circles mark the "contact frequency" $f_{cont} = \mathcal{C}^{3/2}/(2\pi\bar{M})$ [36], where $\mathcal{C} \equiv \bar{M}/\bar{R}$ is the average compactness, $\bar{R} \equiv (R_1 + R_2)/2$, and $R_{1,2}$ are the radii of the nonrotating stars associated with each binary.

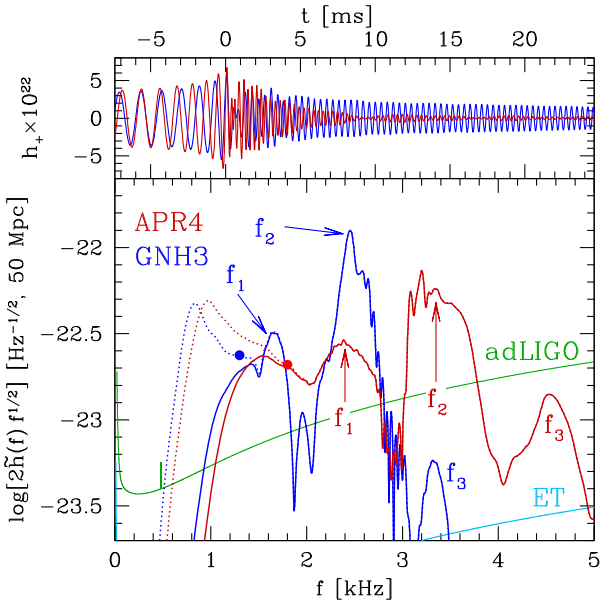

FIG. 1 (color online). Top panel: Evolution of h_+ for representative binaries with the APR4 and GNH3 EOSs (dark-red and blue lines, respectively) for sources at a polar distance of 50 Mpc. Bottom panel: Spectral density $2\tilde{h}(f)f^{1/2}$ windowed after the merger for the two EOSs and sensitivity curves of Advanced LIGO (green line) and ET (light-blue line); the dotted lines show the power in the inspiral, while the circles mark the contact frequency.

Note the clear appearance of two main peaks, indicated as f_1 and f_2, with the first one being smaller in amplitude, but also at frequencies where the detectors are more sensitive. The f_2 peak was named f_{peak} in Refs. [11,13] and f_2 in Ref. [15]. When comparing our values of f_2 with the corresponding ones from Ref. [11] for the same binaries, we have found differences of the order of a few percent at most, thus confirming that the conformally flat approximation provides a rather accurate description of the dynamics of the HMNS. The amplitude of the GW emission, on the other hand, is ~6–9 times larger than in Ref. [11]. We should also note that Ref. [15] reported the presence of two additional frequencies, dubbed $f_- < f_2$ and $f_+ > f_2$, where f_- was tentatively attributed to a nonlinear interaction between the quadrupole and quasiradial modes. We share this interpretation and, as already done in Ref. [10], recognize f_1 (and thus f_- of Ref. [15]) as produced by the nonlinear oscillations of the two stellar cores that collide and bounce repeatedly right after the merger. A larger uncertainty is associated with the physical interpretation of the third and very high-frequency peak, which is indicated as f_3 in Fig. 1. Additional work is needed to explain this mode, which could be an overtone or the result of the nonlinear interaction of the f_2 mode with other nonquasiradial modes.

Although clearly recognizable, we have preferred to use an automatic evaluation of the peak frequencies using a prescription similar to the one discussed in Ref. [31], where

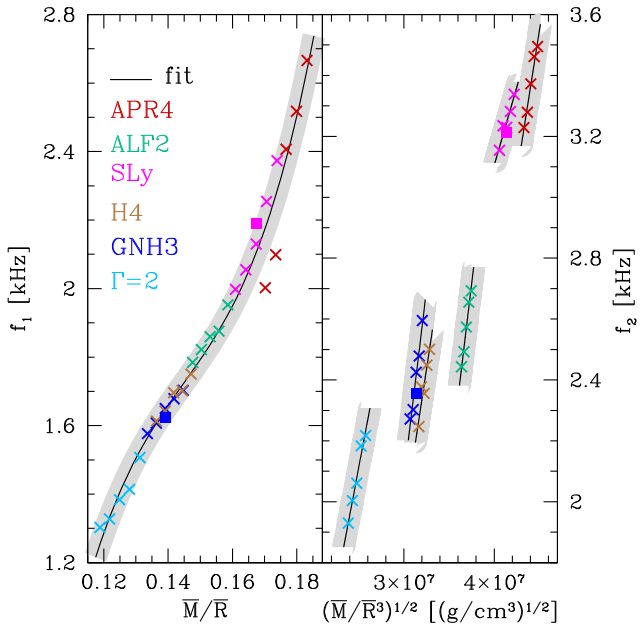

FIG. 2 (color online). Left panel: Fitted values of the low-frequency peaks as a function of the stellar compactness for the six different EOSs considered; note the universal behavior exhibited also by unequal-mass binaries (filled squares). Shown as a solid black line is the cubic fit, while the gray band is the estimate of the total errors. Right panel: Fitted values of the high-frequency peaks as a function of the average rest-mass density; no universal behavior appears.

a fit of the PSDs is performed using two different Gaussian profiles for the two peaks. Details on the fitting procedure of the PSD and the associated errors will be presented in the longer paper [28].

The most interesting and important result of our spectral analysis is that there is a very clear correlation between the low-frequency peak f_1 and the compactness $\mathcal{C}$. The results of the fitting procedure for the low-frequency peak are collected in the left panel of Fig. 2, where the values of the fitted f_1 frequencies are plotted as a function of $\mathcal{C}$ for the various EOSs and are indicated with different colors. Note that the plot displays high-accuracy data for 32 BNSs (the unequal-mass binaries appear as filled squares) and thus collects the results of one year of computing time. Also shown as a shaded gray band is the estimate of the total error, which is effectively dominated by the fitting procedure of the PSD. Postponing to the longer paper the details of the error budget, we anticipate here that the average numerical error from the simulations is 0.06 kHz, while the average uncertainty in the fitting procedure of the PSD is of 0.2 kHz (see also Ref. [31]).

The behavior of the low-frequency peak is remarkably consistent with a simple polynomial function and we have found that a cubic polynomial provides the best fit (solid black line). In this case, the chi-squared value measured is 0.09, with a fitting uncertainty $\lesssim$0.06 kHz; even if the data relative to the APR4 EOS have the largest scattering, all simulations are very well reproduced by the fit within the error bars. The essentially universal behavior of the f_1 frequency with compactness is reminiscent of another universal behavior shown by the orbital frequency at the peak of the GW amplitude [32,37] and provides a powerful tool to constrain the EOS. This is because once a measurement of f_1 is made, the fitting provides a relation of the type $\bar{M} = \bar{M}(\bar{R}, f_1)$, which intersects in just one point in the $(\bar{M}, \bar{R})$ plane the relation $\bar{M} = \bar{M}(\bar{R})$ built for each EOS through equilibrium nonrotating models (cf. Fig. 3 and see discussion below).

Shown instead in the right panel of Fig. 2 is the behavior of the high-frequency peak f_2 as a function of the average rest-mass density $(\bar{M}/\bar{R}^3)^{1/2}$ for the different EOSs. (A correlation with $\mathcal{C}$ is present also for the f_2 frequency, but with a much larger scatter, making it difficult to use to obtain robust and independent information. Correlations are also possible between f_2 and other quantities such as the stellar radius at fixed mass [11,13,14], but again with a large scatter and strong dependence on the EOS.) A similar plot of f_2 as a function of $(\bar{M}/R^3_{\rm max})^{1/2}$, where $R_{\rm max}$ is the radius of the maximum-mass nonrotating configuration, was presented in Ref. [11], where only one mass was considered for the different binaries, but a larger set of EOSs was used. Overall, the mass dependence in f_2 (i.e., what distinguishes different points of the same color) does not suggest a tight universal correlation in our data. Hence, we perform a linear fit for each EOS, reproducing the data rather well (the chi-squared value is $\lesssim$0.004). Although EOS dependent, these fits still provide a set of relations $\bar{M} = \bar{M}(\bar{R}, f_2; \mathrm{EOS})$, which will again intersect at just one point the sequences of equilibrium nonrotating models for each EOS (cf. Fig. 3).

Armed with the correlations described above, we now discuss how to use them to constrain the EOS. Let us assume that the GW signal from a BNS has been detected and that the source is sufficiently close that all of the spectral features are clearly identifiable. [A "clear identification" will need a high signal-to-noise ratio (SNR) and will depend on the EOS; for those in Fig. 1, a realistic SNR = 5 of Advanced LIGO for f_1 implies sources at distances of ~25(~40) Mpc for the APR4 (GNH3) EOS; large distances of ~50(~115) Mpc are possible for f_2.] Using the measured values of f_1 and f_2 we can draw on the $(\bar{M}, \bar{R})$ plane a series of curves given by the relations $\bar{M} = \bar{M}(\bar{R}, f_1)$ (solid gray line) and $\bar{M} = \bar{M}(\bar{R}, f_2; \mathrm{EOS})$ (solid colored lines). This is shown in Fig. 3, where the left panel refers to the ALF2 EOS, while the right one refers to the APR4 EOS. Concentrating on the left panel, we can see that the $\bar{M} = \bar{M}(\bar{R}, f_1)$ relation intersects each of the various equilibrium curves (colored dashed lines) at one point (e.g., at $\bar{M} \simeq 1.325 M_\odot$, $\bar{R} \simeq 12.3$ km for the ALF2 EOS), but also other crossings take place for the other EOSs. However, when using also the relations $\bar{M} = \bar{M}(\bar{R}, f_2; \mathrm{EOS})$, some EOSs can be readily excluded (e.g., APR4, SLy, and GNH3, in our example) and only the

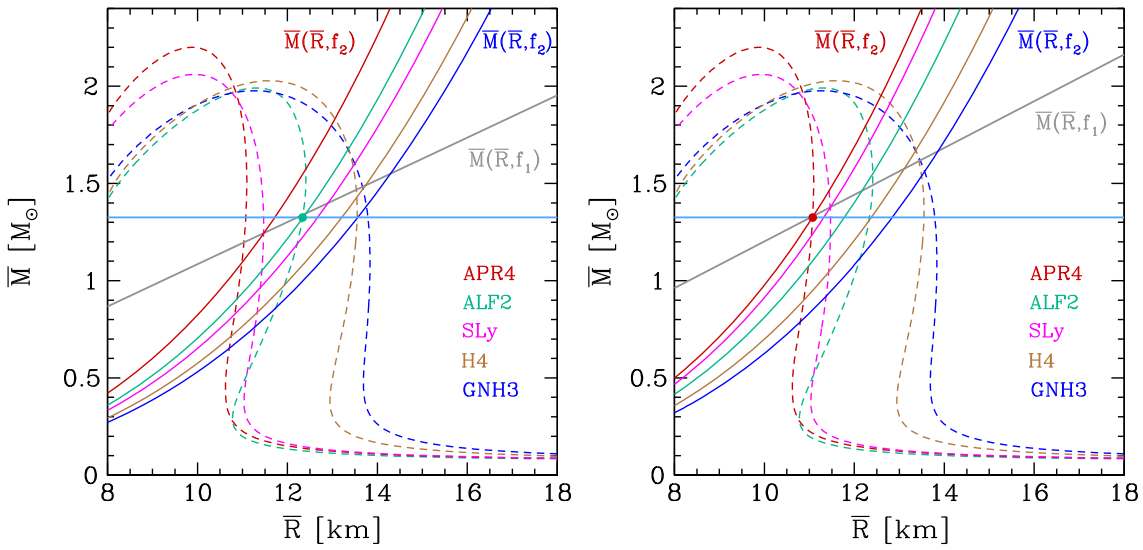

FIG. 3 (color online). Examples of use of the spectral features to constrain the EOS. Once a detection is made, the relations $\bar{M} = \bar{M}(\bar{R}, f_1)$ and $\bar{M} = \bar{M}(\bar{R}, f_2; \mathrm{EOS})$ (colored solid lines) will cross at one point the curves of equilibrium configurations (colored dashed lines). Knowledge of the mass of the system (horizontal line) will provide a fourth constraint, removing possible degeneracies. The left and right panels refer to the ALF2 and APR4 EOSs, but all other EOSs behave in the same way.

ALF2 and H4 EOSs have crossings (or "near crossings") between the equilibrium-models curves and the frequency-correlations curves. Realistically, the uncertainties in the measurement of $f_{1,2}$ (including the experimental ones) will make the correlation curves $\bar{M} = \bar{M}(\bar{R}, f_1)$ and $\bar{M} = \bar{M}(\bar{R}, f_2; \mathrm{EOS})$ appear as "bands" with probability distributions rather than thin lines; the crossing will be harder to judge and will require a complete Bayesian probability analysis (see, e.g., Ref. [31]), which is beyond the scope of this Letter; hence, by near crossings we here mean the overlap of different curves in a small region of the $(\bar{M}, \bar{R})$ plane.

Fortunately, the uncertainty can be removed if the mass of the binary is known from the inspiral signal. In this case, in fact, there will be a horizontal line in the $(\bar{M}, \bar{R})$ plane that will break the degeneracy imposing four simultaneous constraints. This is shown with the horizontal light-blue line, which clearly intersects the three curves relative to the ALF2 EOS at one point only (green solid circle). Also in this case, the horizontal line should in reality be replaced by a band with a probability distribution, but from Fig. 2 it is already possible to conclude that the mass needs to be determined with a relative precision that is $\lesssim 10\%$.

Despite the simplifying assumptions, this method shows that even a single detection of a GW signal with high SNR and from which the mass of the binary can be calculated would be sufficient to set tight constraints on the EOS. This approach works well for all of the binaries considered and an additional example is offered by the right panel of Fig. 3, which reproduces a similar construction for the APR4 EOS. Clearly, also in this case four different curves cross essentially at one point.

Of course this method can work as long as there is a sufficient number of detections and the uncertainties in the measure of the frequencies are small. Using the postmerger signal and fixing a realistic $\mathrm{SNR} = 5$, different EOSs and optimally oriented binaries yield a detection horizon of $\sim 20 - 40$ Mpc, which reduces to $\sim 14 - 28$ Mpc for randomly oriented sources. In turn, the latter yields an event rate of ~ 0.01–$0.1\ \mathrm{yr}^{-1}$, which could increase to ~ 0.1–$1\ \mathrm{yr}^{-1}$ for the optimistic estimate of Ref. [4]. We note that if we assume $\mathrm{SNR} = 2$ as in Ref. [11], then our expected event rate is larger by a factor of $(5/2)^3 \simeq 16$. Following Refs. [38] and [13], we have used the Fisher information matrix to estimate the uncertainties in the determination of the peak frequencies when a GW detection is made. In particular, for sources with optimal orientation at 50 Mpc, the uncertainties for adjacent models are in the range $\sim 1 - 100$ Hz, with the upper value being smaller than the one reported in Ref. [11], where distances of 20 Mpc were considered.

A few additional remarks will be given before concluding. First, even if the measurement of the mass is not available from the inspiral, the possible degeneracies mentioned above could be removed with a few positive detections, which would tend to favor one EOS over the others. Second, if only the f_2 frequency is measurable, the approach discussed above can still be used as long as the mass is known; in this case three and not four curves will have to cross at one point. Third, most of our simulations refer to equal-mass binaries, but we expect that $f_{1,2}$ will not be very sensitive to the initial mass ratio; this was already shown by Refs. [11,14] and is confirmed by the two unequal-mass binaries simulated. Fourth, realistic values of the spins should not influence the

frequencies significantly given that the largest contribution to the angular momentum of the HMNS comes from the orbital angular momentum and not from the initial spins of the stars [39]. Finally, because the f_1 peak is produced soon after the merger, it should not be affected significantly by magnetic fields and radiative effects, whose modifications emerge on much larger time scales [40].

Conclusions.—We have carried out a large number of accurate and fully general-relativistic simulations of the inspiral and postmerger of BNSs with nuclear EOSs. This has allowed us to have a comprehensive view of the spectral properties of the complex postmerger GW signal and to highlight the presence of two robust frequency peaks. We have shown for the first time that the low-frequency peaks exhibit a correlation with the stellar compactness that is essentially EOS independent and that can be used to constrain the EOS once the peak is measured. In addition, the combined use of other EOS-dependent correlations from the high-frequency peaks can further constrain the EOS. In principle, if the mass is known from the inspiral and the peaks are clearly measurable, a single detection would be sufficient to set constraints on the EOS. In practice, a few detections will favor statistically one EOS over the others, but a Bayesian analysis is necessary to quantify these probabilities; we leave this to future work.

We thank A. Bauswein, H.-T. Janka, B. Sathyaprash, and N. Stergioulas for useful comments. Partial support comes from the DFG grant SFB/Transregio 7 and by "NewCompStar", COST Action MP1304. K. T. is supported by the LOEWE-Program in HIC for FAIR. The simulations were performed on SuperMUC at LRZ-Munich, on Datura at AEI-Potsdam, and on LOEWE at CSC-Frankfurt.

[1] G. M. Harry, Classical Quantum Gravity **27**, 084006 (2010).
[2] T. Accadia *et al.*, Classical Quantum Gravity **28**, 114002 (2011).
[3] Y. Aso, Y. Michimura, K. Somiya, M. Ando, O. Miyakawa, T. Sekiguchi, D. Tatsumi, and H. Yamamoto, Phys. Rev. D **88**, 043007 (2013).
[4] J. Abadie *et al.*, Classical Quantum Gravity **27**, 173001 (2010).
[5] É. É. Flanagan and T. Hinderer, Phys. Rev. D **77**, 021502 (2008).
[6] L. Baiotti, T. Damour, B. Giacomazzo, A. Nagar, and L. Rezzolla, Phys. Rev. Lett. **105**, 261101 (2010).
[7] S. Bernuzzi, A. Nagar, M. Thierfelder, and B. Brügmann, Phys. Rev. D **86**, 044030 (2012).
[8] D. Radice, L. Rezzolla, and F. Galeazzi, Mon. Not. R. Astron. Soc. Lett. **437**, L46 (2014).
[9] D. Radice, L. Rezzolla, and F. Galeazzi, Classical Quantum Gravity **31**, 075012 (2014).
[10] L. Baiotti, B. Giacomazzo, and L. Rezzolla, Phys. Rev. D **78**, 084033 (2008).
[11] A. Bauswein and H.-T. Janka, Phys. Rev. Lett. **108**, 011101 (2012).
[12] R. Oechslin and H. T. Janka, Phys. Rev. Lett. **99**, 121102 (2007).
[13] A. Bauswein, H.-T. Janka, K. Hebeler, and A. Schwenk, Phys. Rev. D **86**, 063001 (2012).
[14] K. Hotokezaka, K. Kiuchi, K. Kyutoku, T. Muranushi, Y.-i. Sekiguchi, M. Shibata, and K. Taniguchi, Phys. Rev. D **88**, 044026 (2013).
[15] N. Stergioulas, A. Bauswein, K. Zagkouris, and H.-T. Janka, Mon. Not. R. Astron. Soc. **418**, 427 (2011).
[16] D. Brown, P. Diener, O. Sarbach, E. Schnetter, and M. Tiglio, Phys. Rev. D **79**, 044023 (2009).
[17] F. Löffler, J. Faber, E. Bentivegna, T. Bode, P. Diener, R. Haas, I. Hinder, B. C. Mundim, C. D. Ott, E. Schnetter, G. Allen, M. Campanelli, and P. Laguna, Classical Quantum Gravity **29**, 115001 (2012).
[18] L. Baiotti, I. Hawke, P. J. Montero, F. Löffler, L. Rezzolla, N. Stergioulas, J. A. Font, and E. Seidel, Phys. Rev. D **71**, 024035 (2005).
[19] A. Akmal, V. R. Pandharipande, and D. G. Ravenhall, Phys. Rev. C **58**, 1804 (1998).
[20] M. Alford, M. Braby, M. Paris, and S. Reddy, Astrophys. J. **629**, 969 (2005).
[21] F. Douchin and P. Haensel, Astron. Astrophys. **380**, 151 (2001).
[22] N. K. Glendenning and S. A. Moszkowski, Phys. Rev. Lett. **67**, 2414 (1991).
[23] N. K. Glendenning, Astrophys. J. **293**, 470 (1985).
[24] J. S. Read, B. D. Lackey, B. J. Owen, and J. L. Friedman, Phys. Rev. D **79**, 124032 (2009).
[25] L. Rezzolla and O. Zanotti, *Relativistic Hydrodynamics* (Oxford University, New York, 2013).
[26] H.-T. Janka, T. Zwerger, and R. Mönchmeyer, Astron. Astrophys. **268**, 360 (1993).
[27] A. Bauswein, H. T. Janka, and R. Oechslin, Phys. Rev. D **82**, 084043 (2010).
[28] K. Takami, L. Rezzolla, and L. Baiotti (to be published).
[29] E. Gourgoulhon, P. Grandclément, K. Taniguchi, J.-A. Marck, and S. Bonazzola, Phys. Rev. D **63**, 064029 (2001).
[30] E. Schnetter, S. H. Hawley, and I. Hawke, Classical Quantum Gravity **21**, 1465 (2004).
[31] C. Messenger, K. Takami, S. Gossan, L. Rezzolla, and B. S. Sathyaprakash, arXiv:1312.1862 [Phys. Rev. X (to be published)].
[32] J. S. Read, L. Baiotti, J. D. E. Creighton, J. L. Friedman, B. Giacomazzo, K. Kyutoku, C. Markakis, L. Rezzolla, M. Shibata, and K. Taniguchi, Phys. Rev. D **88**, 044042 (2013).
[33] Advanced LIGO anticipated sensitivity curves, LIGO Document No. T0900288-v3, https://dcc.ligo.org/LIGO-T0900288/public.
[34] M. Punturo *et al.*, Classical Quantum Gravity **27**, 194002 (2010).
[35] B. S. Sathyaprakash and B. F. Schutz, Living Rev. Relativity **12**, 2 (2009).
[36] T. Damour, A. Nagar, and L. Villain, Phys. Rev. D **85**, 123007 (2012).
[37] S. Bernuzzi, A. Nagar, S. Balmelli, T. Dietrich, and M. Ujevic, Phys. Rev. Lett. **112**, 201101 (2014).
[38] J. S. Read, C. Markakis, M. Shibata, K. Uryū, J. D. E. Creighton, and J. L. Friedman, Phys. Rev. D **79**, 124033 (2009).
[39] W. Kastaun, F. Galeazzi, D. Alic, L. Rezzolla, and J. A. Font, Phys. Rev. D **88**, 021501 (2013).
[40] B. Giacomazzo, L. Rezzolla, and L. Baiotti, Phys. Rev. D **83**, 044014 (2011).